Layered Composite Entangled Wire Materials Blocks as Pre-Tensioned Vertebral Rocking Columns

Mohammad M Kashani[1], Ehsan Ahmadi[2], Alicia Gonzalez-Buelga[3], Dayi Zhang[4], Fabrizio Scarpa[5]

Abstract

This work focuses on entangled wire materials as an option for use between segments of a novel self-centring bridge pier inspired from the human spine mechanism to increase energy dissipation capability of the pier in rocking. A comprehensive set of free-decay vibration tests was conducted on small-scale columns with and without entangled wire materials. Wooden blocks are used as vertebrae with entangled wire materials as intervertebral disks. The whole system is tied together using a pre-tensioned tendon. Dynamic properties of columns (i.e. frequency and damping ratio) were then identified and compared. It is found that the use of entangled wire materials significantly increases the energy dissipation capacity of the system during rocking. This finding is very encouraging for future use of entangled wire materials composite systems in large-scale testing of the proposed rocking column, while their shear and axial stiffness needs be improved to reduce large shear and axial deformations.

Keywords: Rocking column; entangled wire material (EWM) layers; vertebral bridge pier; accelerated bridge construction

---

[1] Associate Professor, University of Southampton, Faculty of Engineering and the Environment, Southampton, SO17 1BJ, UK (corresponding author), Email: mehdi.kashani@soton.ac.uk

[2] Postdoctoral Research Associate, University of Southampton, Faculty of Engineering and the Environment, Southampton, SO17 1BJ, UK

[3] Senior Research Associate, University of Bristol, Dept. of Mechanical Engineering University of Bristol, Bristol, BS8 1TR, United Kingdom

[4] Associate Professor, School of Energy and Power Engineering, Beihang University, Beijng, China

[5] Professor, Bristol Composites Institute (ACCIS), University of Bristol, Bristol, BS8 1TR, United Kingdom

1. Introduction

1.1 Background

Bridges are critical nodes in any transport network [1]. In seismic regions, post-earthquake functionality of bridges plays a crucial role in expediting rescue services and mitigating casualties. Malfunction of bridges will interrupt the whole transport network, and create enormous economic losses after seismic events ([2],[3]). With growing urban population and rapid development of economics, reliable seismic design of bridges becomes even more important. Furthermore, there are many bridges all over the world which suffer from material ageing and deterioration, and are located in high-seismicity regions ([4],[5],[6]). Material deterioration (for instance reinforcement corrosion in concrete structures) reduces structural safety margin, and thus residual capacity of structures becomes far smaller than the capacity of newly-built structures. Such a pronounced reduction in structural strength requires costly regular maintenance and rehabilitation works [7].

In conventional construction of concrete bridges, piers are cast in place monolithically to the foundation. For integral concrete bridges, piers are monolithically connected to both foundation and deck. As a result, piers crack under lateral movements of the deck, and accelerated deterioration (e.g. chloride-induced corrosion) occurs ([7],[8],[9]). Moreover, when bridges are subjected to dynamic earthquake loading, plastic hinges occur in bridge piers due to structural system of bridges. Therefore, piers are designed to sustain large plastic deformations which provide high energy dissipation during seismic loadings ([10],[11]). However, very large residual post-earthquake displacements are induced in bridge piers, and accordingly, bridges will not be functional after seismic events ([12],[13],[14]). Furthermore, if bridges are ageing, material deterioration significantly reduces their plastic deformation capacity. Therefore, in the past two decades, many studies have been conducted to develop precast structural systems that

are seismically resilient. The precast structural systems are constructed using more durable materials, and can be used in accelerated bridge construction (ABC) ([15],[16],[17],[18]).

1.2 Self-centring rocking bridge piers

From previous studies, it is found that pre-tensioned self-centring rocking segmental bridge piers are an excellent alternative to the conventional bridge construction ([19],[20],[21],[22],[23]). The pier segments providing rocking mechanism not only allow for offsite manufacturing which speeds up construction time (i.e. ABC), but also minimise the residual displacement of the pier under lateral dynamic loading (i.e. seismically resilient) [24]. However, there are two main drawbacks: (1) the rocking mechanism does not provide sufficient damping under seismic loading, and consequently additional energy-dissipating components are required to be added to the bridge pier ([25],[20],[26]). These additional elements provide energy dissipation through large plastic deformations, and thus need be replaced after seismic events. (2) Sever damages to concrete can also be observed in contact areas due to high contact stress on the rocking surfaces. More recently, a new pre-tensioned segmental bridge pier with hybrid sliding-rocking joints was developed ([27],[28],[29],[30],[31]) to address these two main issues, but they still use plastic deformations to provide damping and energy dissipation in the system. Nikoukalam et al. [32] used polyurethane segments at the column ends to accommodate large rotations. However, this column exhibited residual deformations despite using external replaceable energy-dissipating links.

To avoid permanent structural damage from high irreversible plastic deformations, a biologically-inspired bridge pier was introduced by Kashani and Gonzalez-Buelga [33]. The research presented in this paper is building on the initial idea reported in [33]. Figure 1 illustrates the proposed small-scale pre-tensioned segmental bridge pier considered for a proof of concept study in this paper. The idea was motivated by the mechanics of the human spine. Small square wooden blocks were used to imitate the *'vertebral body'* in the system, and thin

rubber layers were used to simulate the *'intervertebral discs'* (see Figure 1). The whole system then tied together using a stainless still pre-tensioned tendon. The sliding mechanism was negligible due to increased friction between rubber layers and wooden blocks. The significant rocking mechanism in the proposed system was provided by the whole system (blocks as well as tendon) and rubber layers (see Figure 1). It was found that the proposed vertebral system provides desired rocking behaviour under dynamic base excitation. However, rubber layers did not provide sufficient energy dissipation. Clearly then, the proposed novel system lacks an efficient material as the intervertebral disks to improve damping level of the system.
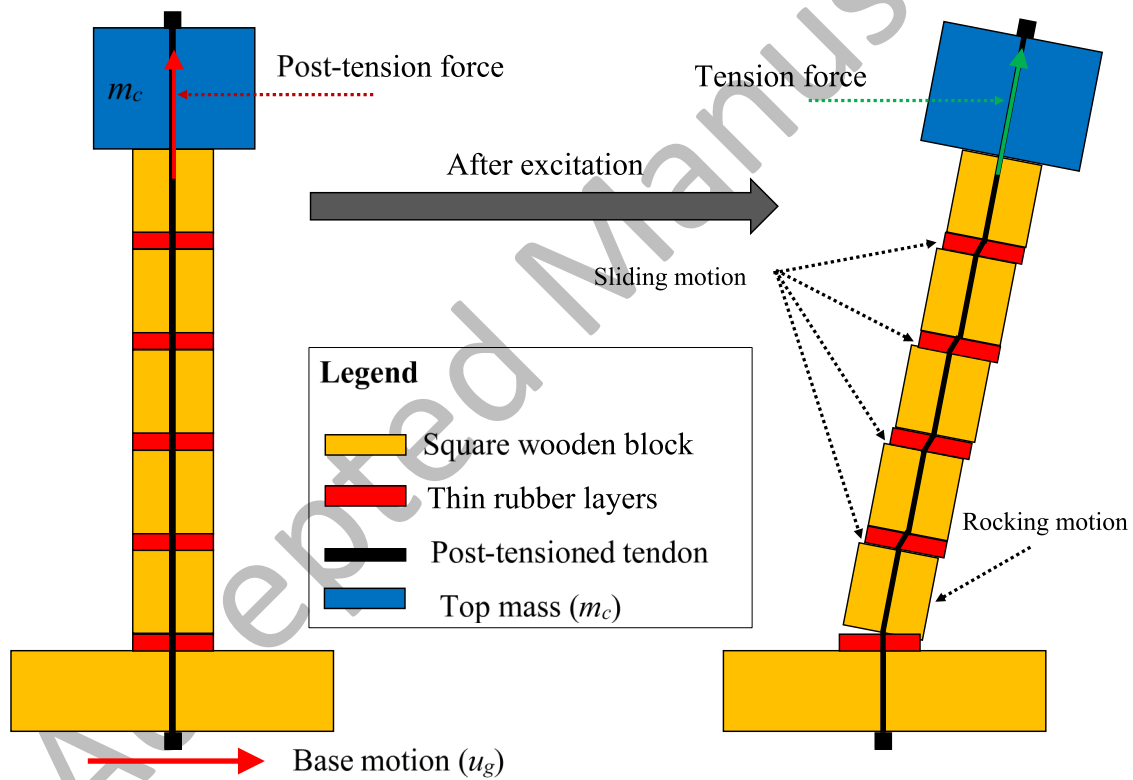

Figure 1. The biologically-inspired bridge pier concept [33].

1.3 Entangled wire material

Entangled wire materials (EWMs – also called metal rubber) are widely used in the aerospace industry as dampers in pipes and gas turbine engines. Theoretically, EWMs have almost zero Poisson's ratio which allows the material to retain its shape with no lateral expansion during

compression [34]. Furthermore, EWMs are also considered as a good shock-absorbent material due to its favourable fatigue life and high damping. These properties make EWMs a potential alternative for use in the biologically-inspired bridge pier as intervertebral disks.

Damping effects of EWMs are highly dependent on internal frictions and contact/slip-stick states within the material [35]. Zhang et al. ([36],[34]) investigated dynamic behaviour of nickel-based EWMs subjected to compressive loading. The results demonstrated high potential of nickel-based EWMs for vibration damping and energy dissipations. Dynamic shear behaviour of nickel-based EWMs was also investigated [37], and considerable energy dissipation under dynamic shear forces were observed too. Zhang et al. [36] classified interaction between metal wires into three phases: non-contact, slip, and stick. At small vibrational amplitudes, wires remain in the stick phase, where static friction is dominant over sliding friction [36]. This has a significant effect on the material loss factor which indicates the energy dissipation through internal friction [38]. At higher vibrational amplitudes, wires begin to change from the stick phase to the slip phase, and the loss factor may decrease as dynamic friction coefficient is lower than static friction coefficient [35]. Therefore, dynamic performance of EWMs under large deformations needs be investigated for their potential use in the novel biologically-inspired bridge pier. Entangled metal wires have multifunctional applications, and have been also recently proposed as energy dissipating units in tensegrity prisms systems ([39],[40]). It is worth noticing that tensegrity prism does possess mechanical behaviours similar to the human spine [41], and also offers interesting static and dynamics performance in a lightweight design in civil constructions [42],[43],[44]. The significant hysteresis effect and modal damping ratio shown by the use of EVMs also in these tensegrity spine-mimicking structures indicate a potential beneficial use of metal rubbers in other composite designs for structural applications.

1.4 Innovation and contribution

Although the proof of concept study on the rocking behaviour of the novel biologically-inspired bridge pier showed promising results, an alternative material to the rubber layers is needed to increase energy dissipation capacity in the system. Therefore, this study addresses this knowledge gap and employs entangled wire materials (EWMs) as an alternative material for use as intervertebral discs. To assess dynamic performance of the system, free-decay vibration tests are conducted on a small-scale simplified vertebral column (with varying EWM arrangements and post-tension force of the tendon) to characterise nonlinear dynamic properties of the system. This work is a preliminary study to lay the scientific foundation for further development of this novel system to be tested at large scales for potential use in engineering practice.

2. Experimental Programme

Free-decay vibration gives useful insight into overall nonlinear behaviour of systems and their frequency and damping variations [45]. Backbone curves and damping skeletons ([46],[47],[48]) can be estimated from free-decay vibration tests particularly for lightly damped systems [45], which are very beneficial to identifying nonlinear dynamics of a system. Cheng [24] used free-decay vibration tests to examine energy dissipation capability of rocking precast bridge piers. Therefore, the experimental programme in this study mainly comprises an ensemble of free-decay vibration experiments on the proposed self-centring segmental column (see Figure 1) with different arrangements of EWM layers. Prior to main free-decay vibration tests, some quasi-static displacement control pullover tests were also conducted to get an insight into force-displacement behaviour of each column.

2.1 Description of small-scale composite columns

The small-scale self-centring segmental columns tested in this study are shown in Figure 2. It consists of a base, a column, a tendon, and a mass on the top. Ten number of 60 mm square

wooden blocks were used to model the *'intervertebral bones'* and nickel-based EWM layers (see Figure 3) were used to simulate *'intervertebral discs'*. A 35 N mass on the top of the column was used to represent the deck of bridges, which generates the inertia forces. A 3 mm hole was drilled through the centre of each block and each EWM layer to allow for a 1.5 mm high-strength stainless pre-tensioned tendon. The tendon provides structural integrity and self-centring capability of the whole system. The tendon was connected to a load cell through a clamp at the top of the column. A bottom clamp was also used to connect the column to the base. The initial pre-tensioning force of the tendon could be adjusted using an adjustable screw, which was connected to the tendon. The initial post-tension force of the tendon was provided by hanging weights (15-52 kg) on a knot at the bottom clamp and spinning the knot. Four counterbores were drilled to bolt the base to a stable underneath table.

Figure 2. (a) Image of an entangled metal wire (EVM) sample used in the composite intervertebral disk, and (b) Example of small-scale self-centring vertebral columns with six intervertebral discs.
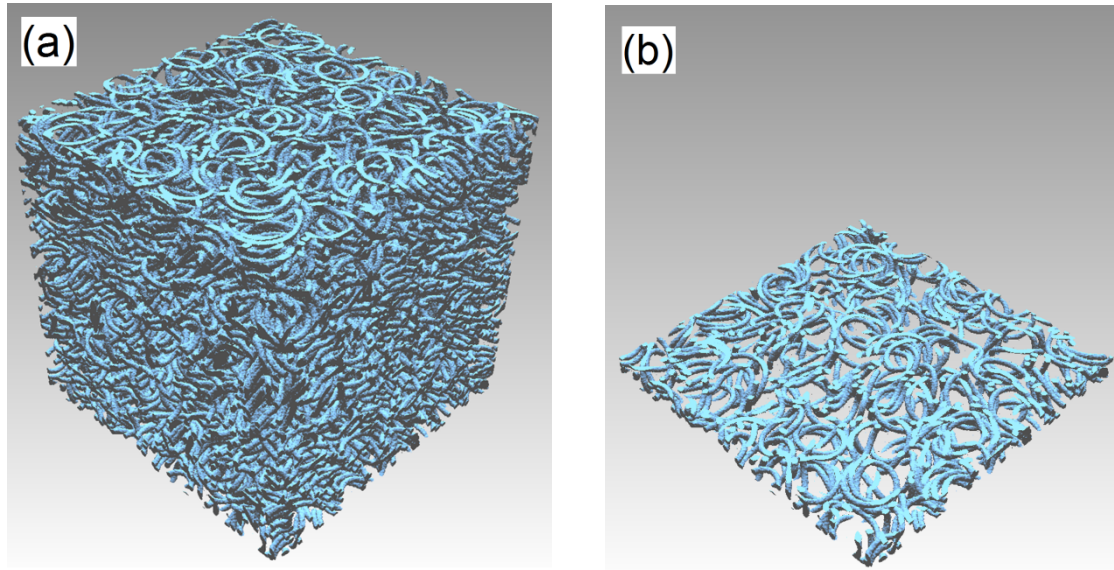
Figure 3. (a) 3D image of the internal volume of a MR sample (10mm*10mm*10mm) from a μ-CT scan (b) Detail of one slide of the internal volume [34].

$51.5 \times 51.5 \times 5.3$ mm nickel-based EWM layers with porosity, mass, and shear force of 80%, 21.5 gr, and 67 kN were used. The height is defined along the moulding direction during the manufacturing. The same direction represents also the one related to the length direction in Figure 3b. The relative density is defined as the ratio between the EWM's and the wire's densities, i.e. the density of the 0Cr18Ni9 material, equivalent to $7.93 g/cm^3$. The EWM layers are placed between bottom wooden blocks as rocking moments and deformations are higher at the base. Four different EWM layer arrangements were used to investigate the influence of EWM layers on the dynamic behaviour of the column: (1) no EWM layers, (2) two EWM layers, (3) four EWM layers, and (4) six EWM layers between wooden blocks (see Figure 4). These columns are respectively referred to as C0, C2, C4, and C6 hereafter where the numbers indicate number of EWM layers.
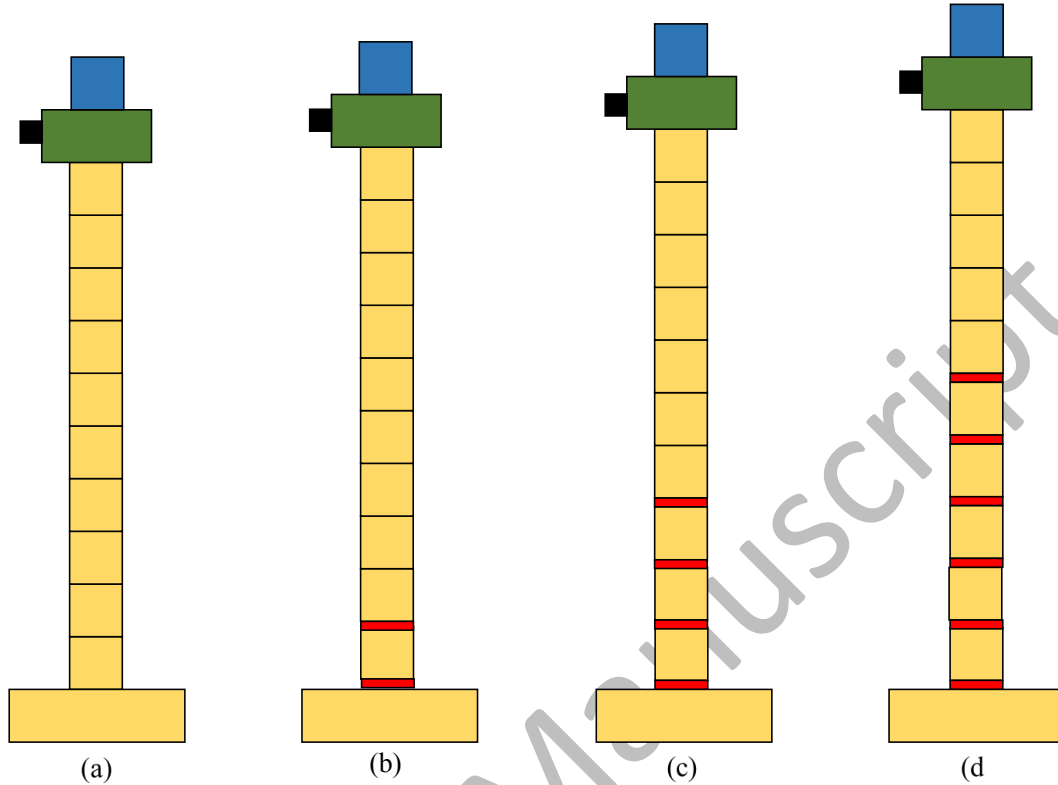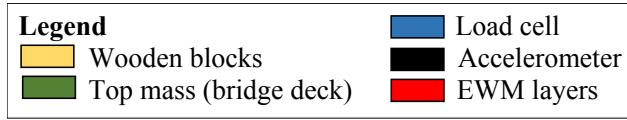
Figure 4. Different arrangements of EWM layers: (a) no EWM layers (i.e. C0), (b) two EWM layers (i.e. C2), (c) four EWM layers (i.e. C4), and (d) six EWM layers (i.e. C6).

2.2 Free-decay vibration test

To conduct a free-decay vibration test on each of the columns (see Figure 4), the tension force of the tendon was first set to an initial value, T_i. Then, the column was laterally pulled, and the increase in the tendon force was monitored until it reached a target tension force, T_t. Afterwards, the column was released to vibrate and the acceleration on top of the column, a_c, as well as the tendon tension force, T_c, were measured.

There different types of free-decay vibration tests were conducted on the columns:

- **Test 1**: To see how initial tension force of the tendon affects dynamic behaviour of the column, C0, the T_i was incrementally increased from 150 N to 300 N by 20 N. For each initial tension force, the column was pulled ten times with a constant target tension force, $T_t = 400$ N. The range of target tension force was chosen based on results of a

number of pullover tests conducted on each column. Results of pullover tests will be discussed in Section 3.1.

- **Test 2**: To see how target tension force of the tendon influences dynamic behaviour of the column C0, for the same initial tension force as the Test 1, the target tension force was incrementally increased ten times up to 400 N.

- **Test 3**: To investigate dynamic behaviour of C2, C4, and C6 columns, the initial tension force of the tendon was set to a constant value. The same initial tension force as the maximum for the C0 column, T_i = 300 N, was first used. The columns were stayed at where it was pulled to because the EWM layers deformed, and the tension force of the tendon reached an equilibrium point. Therefore, the initial tension force of the tendon was increased to a tension force of 500 N, and the columns were able to move back to their initial position. The target tension force was increased from 520 N to 600 N by 20 N.

2.3 Instrumentation, calibration and data collection

A 2.5 kN tension/compression load cell (Model MCL, Universal Load Cell from RDP [49]) and a PBC accelerometer (model 333M07 [50]) with measurement range of ±10g and sensitivity of 99 mV/g were accurately calibrated and used to record the post-tension force in the tendon and in-plane lateral acceleration of the columns respectively. The load cell was calibrated by incrementally increasing the weight on the hanger and recording the corresponding value. Figure 5 shows the original weight-voltage values and a line fitted to the data. The gain (i.e. slope of fitted line) and offset (i.e. voltage axis intersect) are 254 N/V and 0.007 V.
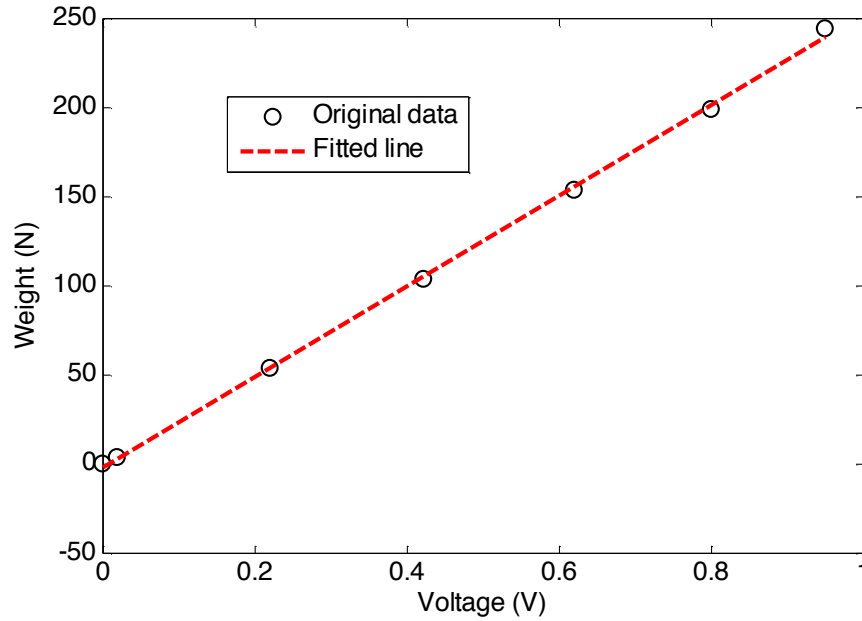
Figure 5. Load cell calibration, weight versus output voltage.

The accelerometer was calibrated by a Type 4294 Brüel & Kjær calibration exciter. It is driven by a crystal oscillator and constantly sends steady sinusoidal signal. The calibration process was then to offset the signal and calculate the gain to reach a gravity acceleration. The accelerometer was connected to a signal conditioner with a gain 100. The offset was 0 and the gain was 10^3 ms^{-2} /V.

The load cell was connected to a Modular 600 Multi-Channel Signal Conditioning System and then to a dSPACE controller [49]. The accelerometer was connected to a 4 Channel Piezoelectric Sensor Power Supply & Signal Conditioner and then to the dSpace controller. The dSPACE Control Desk was programmed in MATLAB Simulink [51] to collect tension force and acceleration signals shown in Figure 6. Each signal was recorded for 10 seconds with sampling frequency of 10^3 Hz.
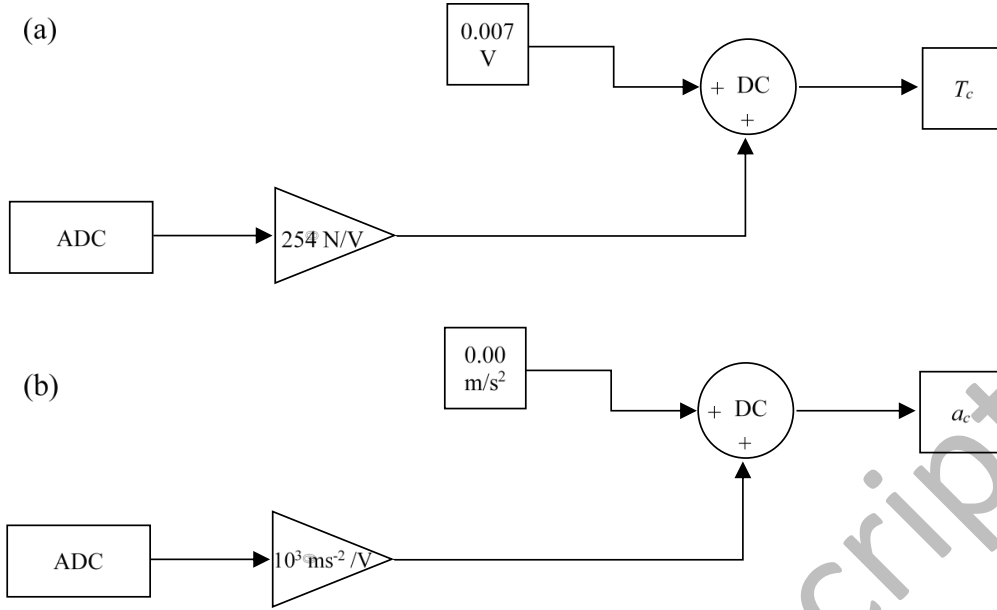
Figure 6. Diagram of the data acquisition model: (a) tension force of the tendon, and (b) acceleration of the column (ADC and DC respectively stand for analogue to digital convertor and dSpace controller).

3. Experimental results

In this section, displacement control tests results as well as original measured tension force and acceleration signals from free-decay vibration tests are presented, and processed for further analysis in Section 4 of this paper. It should be noted that free-decay tests for C0 with $T_i =$ 150 N and $T_t = 390$ N as well as C2 with $T_i = 500$ N and $T_t = 580$ N are used as examples to demonstrate the data analysis procedure and experimental results throughout the paper, and hereafter they are referred to as "*exemplar tests*".

3.1 Displacement control tests on all columns

Prior to main experimental tests (i.e. free-decay vibration tests), displacement control tests were carried out to capture overall tendon tension force versus column's tip displacement (i.e. T_c - D_c curves) behaviour for each specimen. These curves provide good insight into the ranges of initial and target tension force of the tendon taken for the main free-decay vibration tests. For the column C0, the initial tension force of the tendon was increased from 150 N to 300 N by 20 N. For columns C2, C4, and C6, the initial tension of the tendon was set 500 N.

The displacement is normalized by column height and referred to as drift ratio (D_c/h_c). The tension force of the tendon is normalised by its initial tension force, and named here as tension force ratio (T_c/T_i). Figure 7 shows the tension force ratio versus drift ratio curves for all types of columns. All columns, either with or without EWM layers, exhibit a dynamic softening, meaning that columns become less stiff as they displace further ([47],[52]). The nonlinearity in the stiffness (i.e. slope of each force-displacement curve) at small drift ratios is clearly seen. In general, the columns behave linearly until the first joint opens (the first base block), and then show a strength hardening behaviour with reduced stiffness due to joint opening. As seen in Figure 7a, increasing initial tension force of the tendon delays the joint opening and increases the strength hardening. However, it does not affect the stiffness of the system (i.e. constant slopes, 0.52 N/mm). This is in good agreement with the analytical solution of a single tied rocking block derived by Alexander et al. [53]. As evident from Figure 7b, adding EWM layers significantly changes tension force ratio-drift ratio behaviour of the column. Comparing to C0 column, columns with EWM layers show a much lower stiffness, respectively 0.18 N/mm, 0.11 N/mm, and 0.07 N/mm for post-joint opening branch (i.e. at large displacement drift ratios).
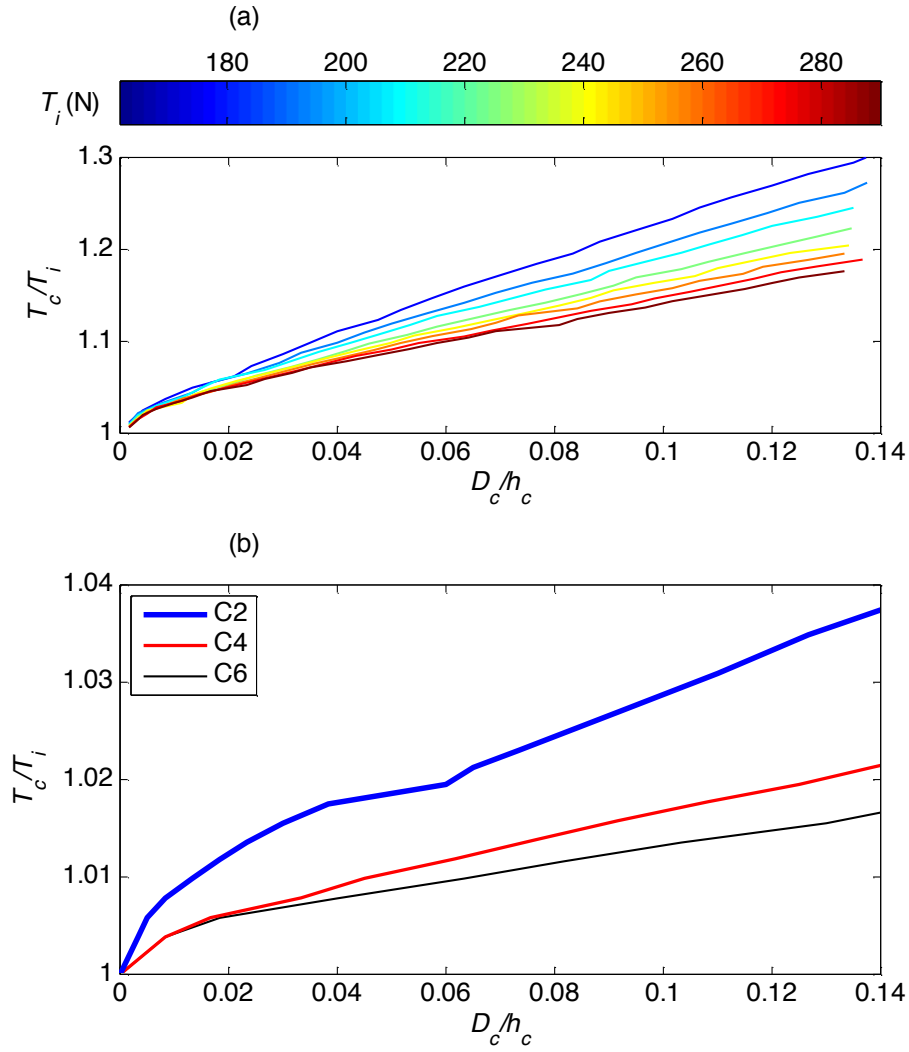
Figure 7. Tendon force ratio-column drift ratio curves: (a) C0 column, and (b) C2, C4, and C6 columns.

3.2 Free-decay vibration test on column C0

Figure 8a shows auto-spectral density (ASD) of the accelerometer for the exemplar C0 test. The ASD can be seen to have high amplitudes around the first rocking mode frequency of the column (2.8 Hz-shown by vertical red dashed line in Figure 8a). The side frequency peaks near the main resonance peak demonstrate the nonlinearity of the system due to friction between blocks before joint opening (e.g. small vibration amplitudes). This will be investigated further in Section 4 using backbone curves. The ASD also shows that most of the column vibration energy is distributed in the frequency range 2-6 Hz and originates from the first rocking mode

of the column. Thus, the low-magnitude high-frequency components of the acceleration response are removed for all C0 tests using a zero-phase 4th order low-pass Butterworth filter [54] (see Figure 8b) with cut-off frequency, 15 Hz. Zero-phase filtering avoids any time shift in the filtered signal.

Figure 8c shows ASD of the tendon force signal for the exemplar C0 test. The ASD exhibits a maximum at the tendon tension frequency, (0.1 Hz-shown by vertical red dashed line in Figure 8c). The ASD shows that most of the tendon vibration energy is concentrated in the frequency range 0-1 Hz. Thus, the higher-frequency components of the tendon force are removed for all tests using a zero-phase 4th order low-pass Butterworth filter (see Figure 7d) with cut-off frequency, 5 Hz. It should be noted that both acceleration and force signals clearly demonstrate that all C0 columns exhibit a typical oscillatory and underdamped free-decay vibration behaviour.
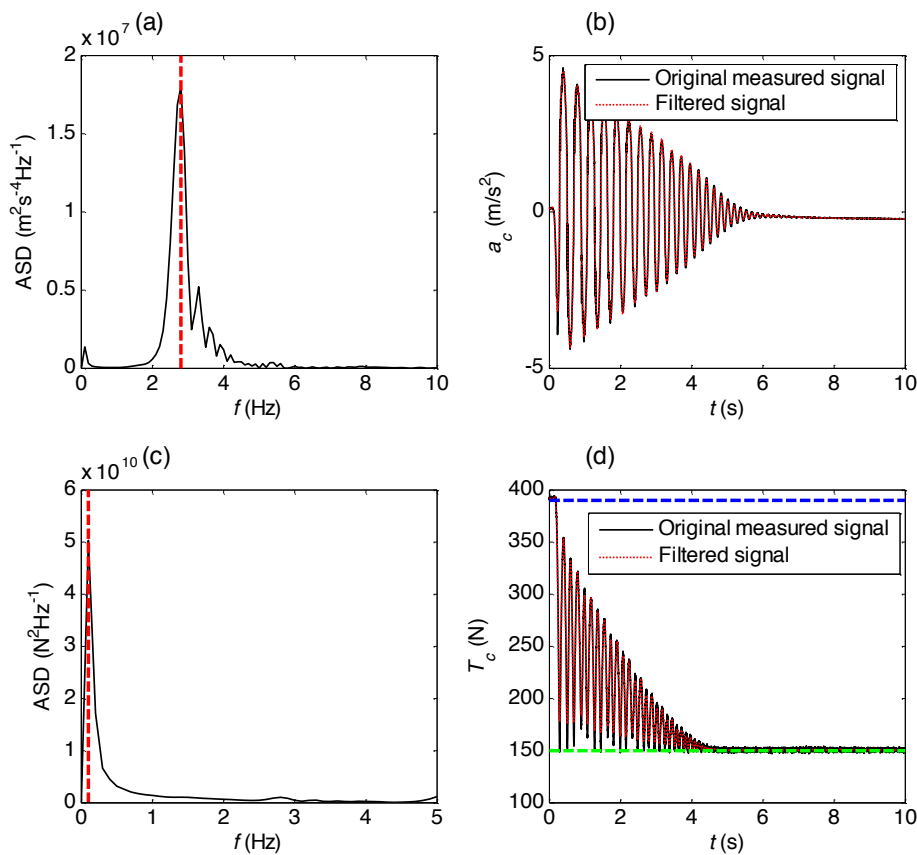
Figure 8. For the exemplar C0 test: (a) frequency content of the acceleration response, (b) acceleration response at the top of the column, (c) frequency content of the tendon force, and (d) tendon force signal.

3.3 Free-decay vibration test on column C2

Figure 9a illustrates ASD of the accelerometer for the exemplar C2 test. In contrast to C0 tests (see Figure 8a), the ASD here has two different maximum values: (1) at a low frequency, 0.1 Hz, and (2) at a higher frequency, around 1.7 Hz (shown by vertical red dashed lines in Figure 9a). The same Butterworth filter with cut-off frequency of 4 Hz is used here to remove very high-frequency vibrations. The vibration amplitude has a significant drop at the beginning of the free-decay vibration, which implies high damping level of the systems due to EWM layers (see Figure 9b). The free-decay vibration behaviour is similar to overdamped systems with a few vibration cycles, and is completely different to the free vibration of typical underdamped systems.
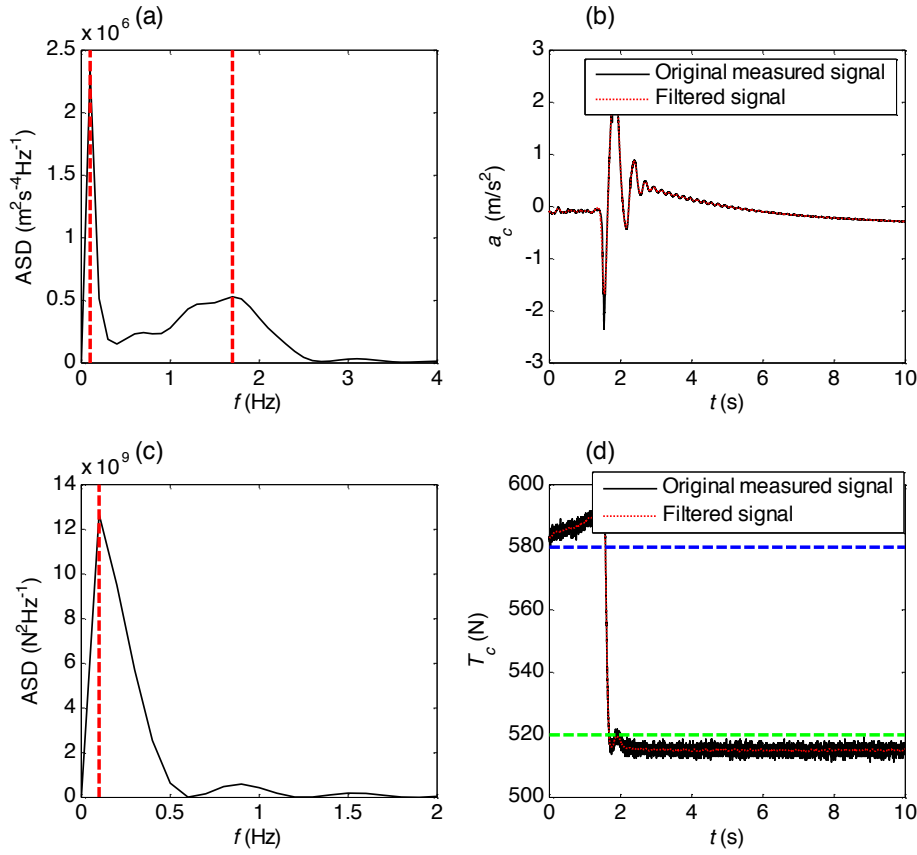
Figure 9. For the exemplar C2 test: (a) frequency content of the acceleration response, and (b) acceleration response at the top of the column, (c) frequency content of the tendon force, and (d) tendon force signal.

As expected, the tendon has the same frequency content as the C0 tests (see Figure 8c). As opposed to the C0 tests where the tendon force drops from the target tension force (390 N-blue dashed line in Figure 8d) to its initial tension force (150 N-green dashed line) in around 5 seconds (see Figure 8d), for the C2 test, however, the tendon force experiences a sudden drop from the target tension force to the initial tension force in less than a second. This fast drop implies the flexibility and highly damped nature of columns with EWM layers compared to those without any material between blocks.

4. Data Analysis

In this section, dynamic properties of the columns (i.e. frequency and damping ratio) are determined from free-decay vibration responses for all tests. As the wooden blocks-to-lump mass ratio is very low (less than 0.0001), the column be idealised with a classical low-order

single degree of freedom (SDOF) system as shown in Figure 10. The rotational spring represents the rocking stiffness of the columns which varies during the motion. The equation of motion for the free vibration of the column can be given by:

$$\ddot{x}_c + 2\xi_c \omega_n \dot{x}_c + \omega_n^2 x_c = 0 \tag{1}$$

where $\ddot{x}_c$, $\dot{x}_c$, and x_c are acceleration, velocity, and displacement of the mass respectively; $\omega_n = 2\pi f_n$ is circular frequency of the system; f_n and ξ_c are natural frequency and damping ratio of the system.
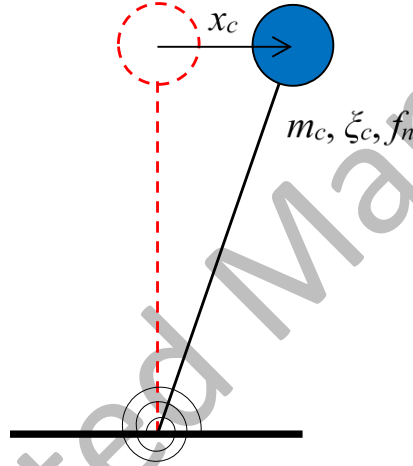

Figure 10. Equivalent SDOF model of the column.

It should be noted that equation (1) holds true for both linear and nonlinear systems. For nonlinear systems, natural frequency and damping ratio of the system are amplitude-dependent and varies between cycles of vibration. The acceleration solution to equation (1) for underdamped systems ($\xi_c < 1$) only for one cycle of vibration is:

$$\ddot{x}_c = e^{-\omega_n \xi_c t} \left(c_1 \cos(\omega_d t) + c_2 \sin(\omega_d t) \right) \tag{2}$$

and for overdamped systems ($\xi_c > 1$):

$$\ddot{x}_c = e^{-\omega_n \xi_c t} \left(c_3 \cosh(\omega_d t) + c_4 \sinh(\omega_d t) \right) \tag{3}$$

where ω_d is damped frequency, $\omega_d = \omega_n \sqrt{\left|1 - \xi_c^2\right|}$; c_1 to c_4 are coefficients depending on initial time conditions of the system. The overdamped solution (i.e. equation (3)) can be represented as the summation of two exponential terms:

$$\ddot{x}_c = c_5 e^{-\omega_l t} + c_6 e^{-\omega_h t} \tag{4}$$

where again c_5 and c_6 are initial condition-dependent coefficients; ω_l and ω_h are named as lower and higher circular frequencies:

$$\omega_l = \omega_n \left(\xi_c - \sqrt{\xi_c^2 - 1} \right) \tag{5a}$$

$$\omega_h = \omega_n \left(\xi_c + \sqrt{\xi_c^2 - 1} \right) \tag{5b}$$

As it is clear from equations (5a) and (5b), response of overdamped systems contains two highly distinctive frequencies (i.e. ω_l and ω_h - see Figure 9a) while response of underdamped systems comprises a discernible frequency (i.e. ω_d - see Figure 8a). It should be noted that the damping and frequency of the column without EWMs are determined from the exponential term for each cycle of vibration. This allows for instantaneous frequency and damping to change with vibration amplitude as would happen in a nonlinear system. As will be discussed in the following section, the damping and frequency are significantly amplitude dependent, which shows the system's nonlinearity. However, for damping model of the column with EWM layers, it will be seen that the system is highly overdamped and viscous damping model is very appropriate.

4.1 Column with no EWM layer

As seen in Section 3.2, experimental results of C0 columns exhibited an oscillatory vibration (i.e. underdamped free-decay vibration). For the underdamped column, the analytical envelopes of the free-decay response are given by ([55], [47]) (see equation (2)):

$$A(t) = A_c e^{-\omega_n \xi_c t} \tag{6}$$

where A_c is the free-decay vibration amplitude at a specific time instant. Following procedure is used herein to determine instantaneous frequency and damping of C0 columns for a specific free-decay vibration response:

1. Trim start and end of the free vibration response and remove its zero-frequency component (static component).

2. Filter the free-decay vibration response using a 4th order low-pass Butterworth filter with cut-off frequency of 10 Hz (see Section 3.2).

3. Identify each vibration amplitude and its corresponding time instant, respectively denoted as $A_{c,i}$ and t_i for the ith vibration amplitude.

4. Determine frequency at time instant, t_i, as $f_{n,i} = 1/(t_{i+1} - t_i)$.

5. To determine damping, $\xi_{c,i}$ at t_i, fit an exponential curve to amplitudes, $A_{c,i}$ and $A_{c,i+1}$, respectively at t_i and t_{i+1}.

Figure 11 shows instantaneous frequency, f_n, damping, ξ_c, and amplitude, A_c, for the exemplar C0 column using steps 1-5 described above. A seen in Figures 11b and 11c, both frequency and damping ratio of the column increase with time. At high vibration amplitudes (4.5 m/s^2 for the exemplar C0 column, see Figure 11d), the column's frequency is 2.7 Hz, and the damping ratio is relatively light, 0.0125. Thus, the free-decay vibration results can be used to estimate backbone curves [45]. To achieve this, displacement amplitudes are determined from acceleration amplitudes at the ith vibration frequency, $\omega_{n,i}$ [45]:
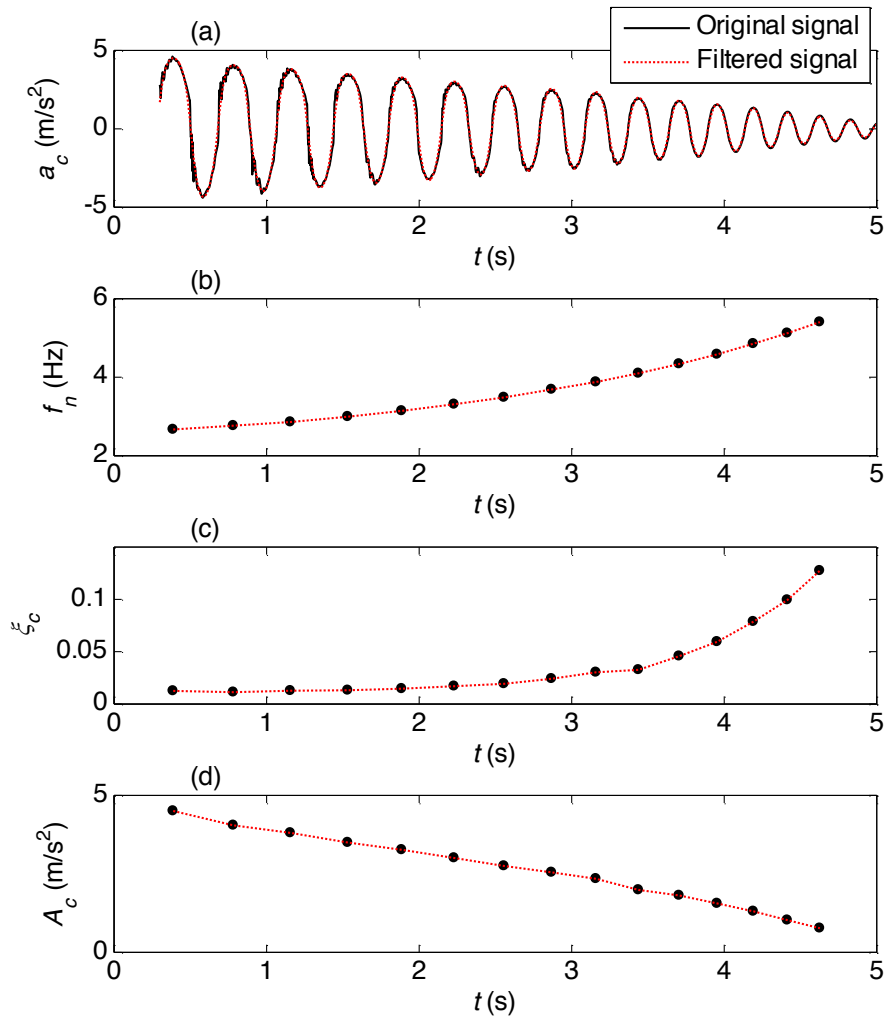
$$D_{c,i} = \frac{A_{c,i}}{\omega_{n,i}^2} \tag{7}$$

Figure 11. For the exemplar no-EWM layer column test: (a) filtered and trimmed acceleration response, (b) instantaneous frequency, (c) instantaneous damping, and (d) vibration envelope.

The amplitude-dependent frequencies of the column, f_n, is normalised by the column's frequency, f_c, at very small vibration amplitudes, where the column frequency is independent on the initial tension force of the tendon. Therefore, the backbone curve is described in terms of drift ratio versus frequency ratio. Figure 12 shows non-dimensional backbone and damping ratio skeleton data for all C0 column tests with different initial post-tension force and constant target tension force (i.e. Test 1). The column frequency decreases with vibration amplitude which is typical in lightly-damped structures [56]. However, the damping ratio decreases with vibration amplitude for the column while for typical structures, the damping ratio increases for

higher vibration amplitudes due to nonlinear damping effects involved. The main reason of this behaviour lies within the tendon's contribution to the integrity of wooden blocks. At high vibration amplitudes, despite the compression force acting on wooden blocks being larger because of higher tensions in the tendon, the friction damping between blocks are insignificant due to the joint opening and rocking. As the column gets closer to its stationary position, the wooden blocks contact area increases, and friction damping increases accordingly.
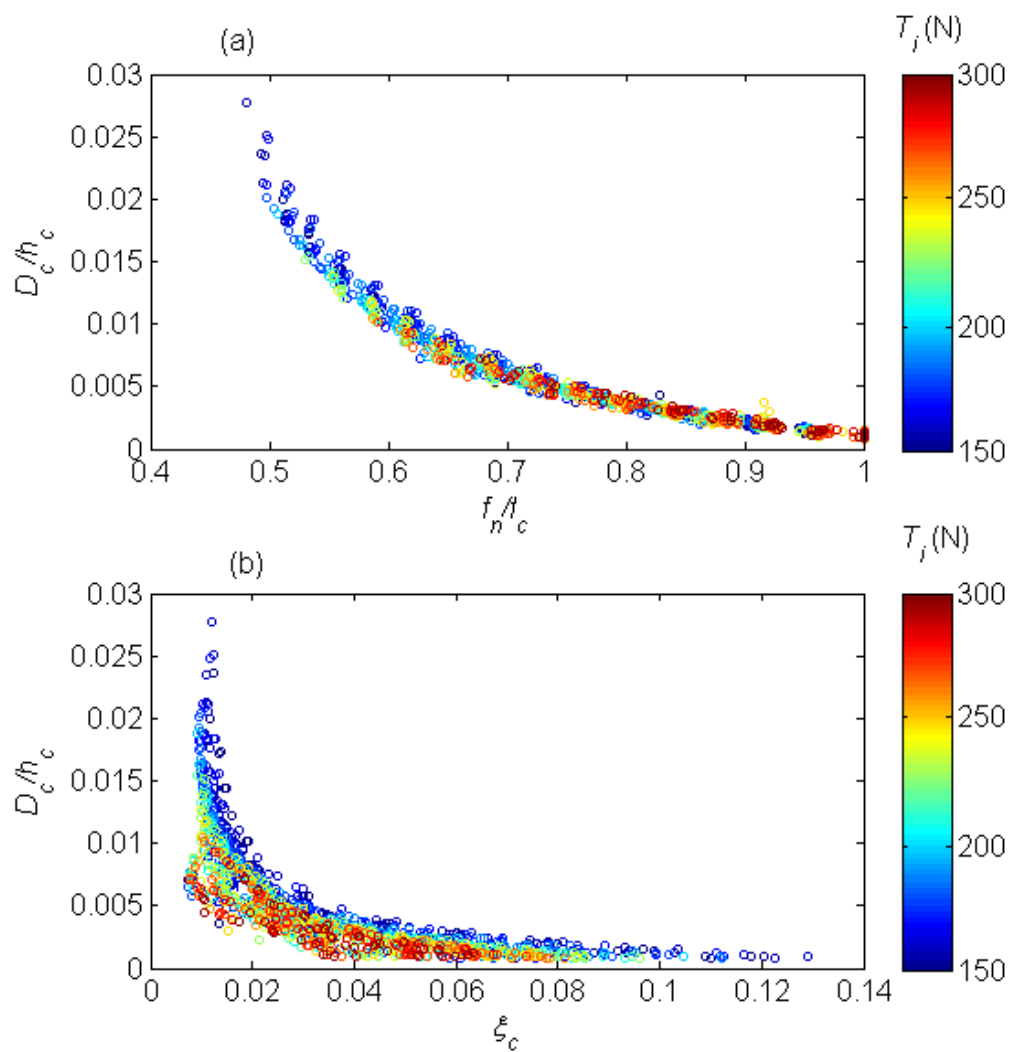

Figure 12. For all C0 column tests with different initial tension force and constant target tension force, $T_t =$ 400 N: (a) backbone estimation data, and (b) damping ratio skeleton data.

The normalised backbone data follows similar trend regardless of initial tension force, and this well shows that initial tension force of the tendon does not influence the stiffness of the column

(see Figure 12a). However, as the initial tension force increases, the damping ratio skeleton

data move towards lower damping ratios (see Figure 12b). Figure 13 shows non-dimensional

backbone and damping ratio skeleton data for all C0 column tests with different initial tension

force and different target tension forces (i.e. Test 2). The results are similar to those with

constant target tension force. This demonstrates that no residual deformation generates in the

system and the tendon tension force brings the column back into to its initial state through
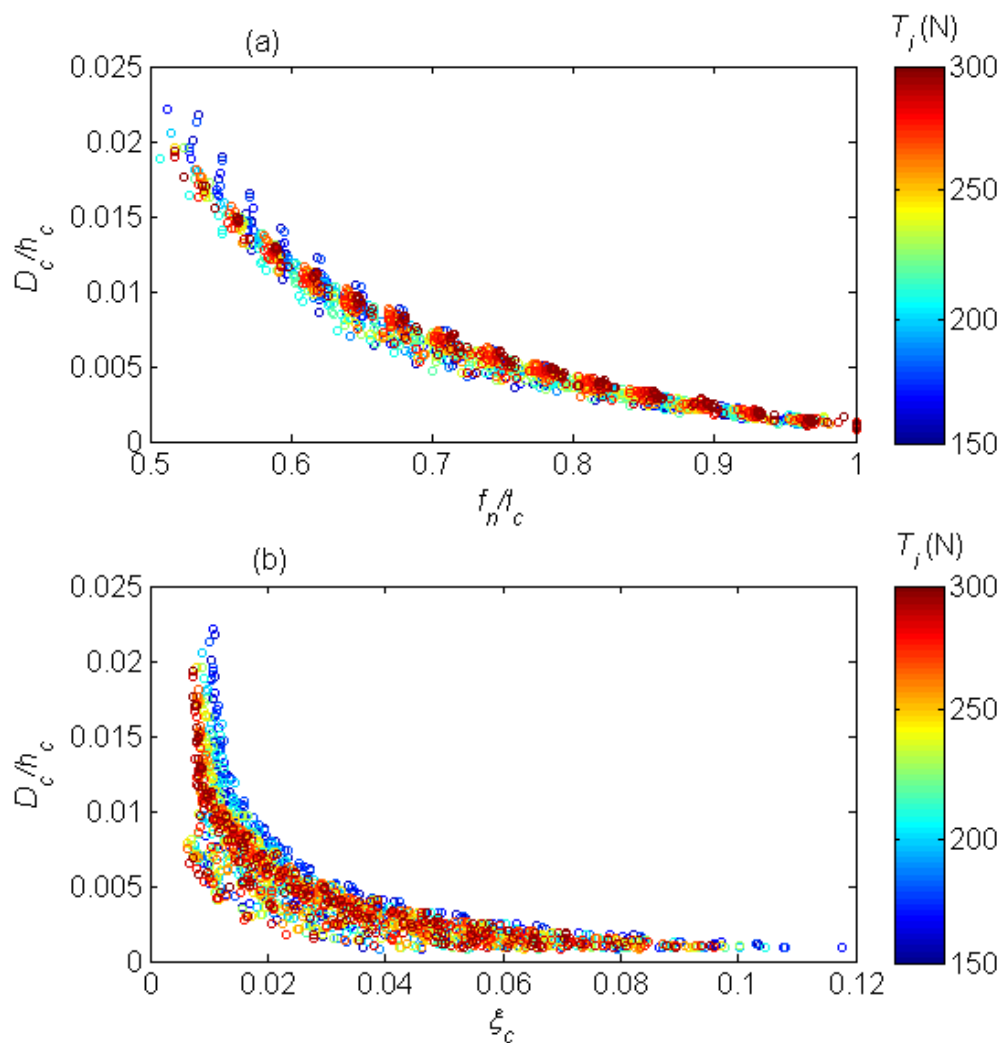
similar force-displacement behaviour.

Figure 13. For all C0 column tests with various initial tension and target tension forces: (a) backbone estimation data, and (b) damping ratio skeleton data.

4.2 Columns with EWM layers

As experimental results of Section 3.3 showed, the free-decay vibration response of the C2 exemplar tests are very close to behaviour of overdamped free-decay systems. Therefore, as the behaviour is non-oscillatory, the backbone and skeleton data cannot be obtained for columns with EWM layers. For the overdamped columns, the total response is the sum of two responses: a lower-frequency response, $\ddot{x}_l(t) = c_5 e^{-\omega_l t}$, and a higher-frequency responses, $\ddot{x}_l(t) = c_5 e^{-\omega_l t}$ (see equation (4)-Section 4). As ASD of acceleration response of the exemplar C2 column test showed (see Figure 8a, Section 3.3), lower frequency of the acceleration response, f_l, is 0.1 Hz, and higher frequency of the acceleration response, f_h, is spread in a frequency band with central frequency of around 1.7 Hz.

To determine the lower-frequency component of the response, $\ddot{x}_l$, a low-pass 4th order Butterworth filter with cut-off frequency of 0.4 Hz is used (see blue dotted line in Figure 14a). Subtracting the lower-frequency response component from the total response then gives the higher-frequency response component, $\ddot{x}_h$ (see red dotted line in Figure 14a).
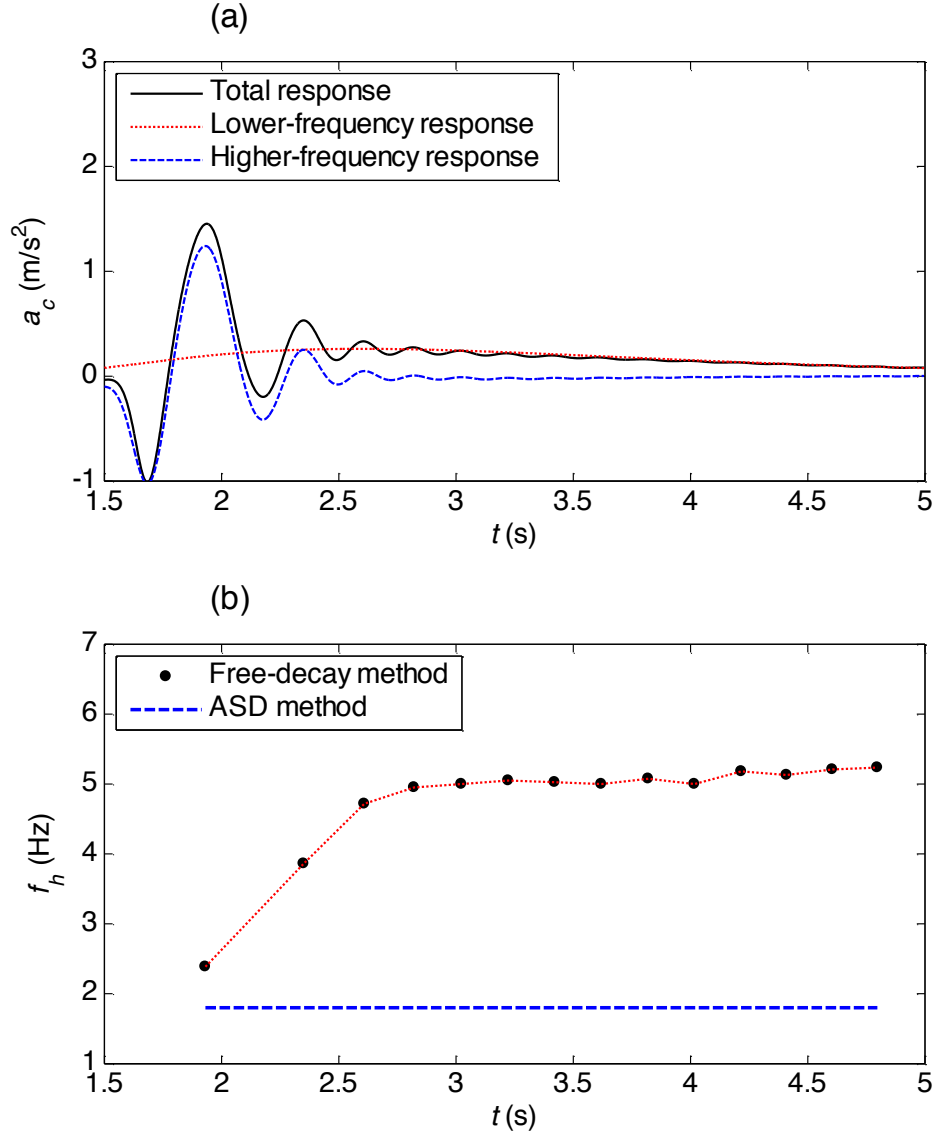
Figure 14. For the exemplar two-EWM layer column test: (a) total acceleration response and its higher- and lower-frequency components, and (b) higher frequency.

It is seen that the higher-frequency response component exhibits an oscillatory vibration with a few cycles of vibration (Figure 14a):

$$\ddot{x}_h(t) = A_h^c e^{-\omega_h t} \qquad (8)$$

Therefore, the same procedure as in Section 4.1 is used here to determine the higher frequency at different vibration amplitudes (see Figure 14b). Figure 14b shows the frequency of the higher-frequency response component from free-decay method as well as from the ASD. As it

is clear, the higher frequency from the free-decay method at large vibration amplitudes is very close to that obtained from ASD method (see Figure 14b, blue dashed line, f_h = 1.7 Hz).

To determine the damping and frequency of the column at large amplitudes, equations (5a) and (5b) are combined:

$$\omega_l + \omega_h = 2\omega_n \xi_c \tag{9a}$$

$$\omega_l \omega_h = \omega_n^2 \tag{9b}$$

f_l and f_h are used in equations (9a) and (9b), which gives ξ_c = 1.9 and f_n = 0.41 Hz. Figure 15 shows the natural frequency and damping for all columns with EWM layers versus different target tension forces. First, the natural frequencies of the columns are far lower compared to the column C0 meaning the columns are more flexible (see Figure 15a). As the number of layers increases, the natural frequency reduces further. Also, the damping of columns with EWM layers is significantly higher than the column without EWM layers (see Figure 15b). This shows high energy dissipation of these columns which dampen the vibration within a few cycles of vibration. Comparing damping ratios of the columns C2, C4, and C6 demonstrate higher capability of the columns with higher EWM layers to dissipate vibration energy as expected.
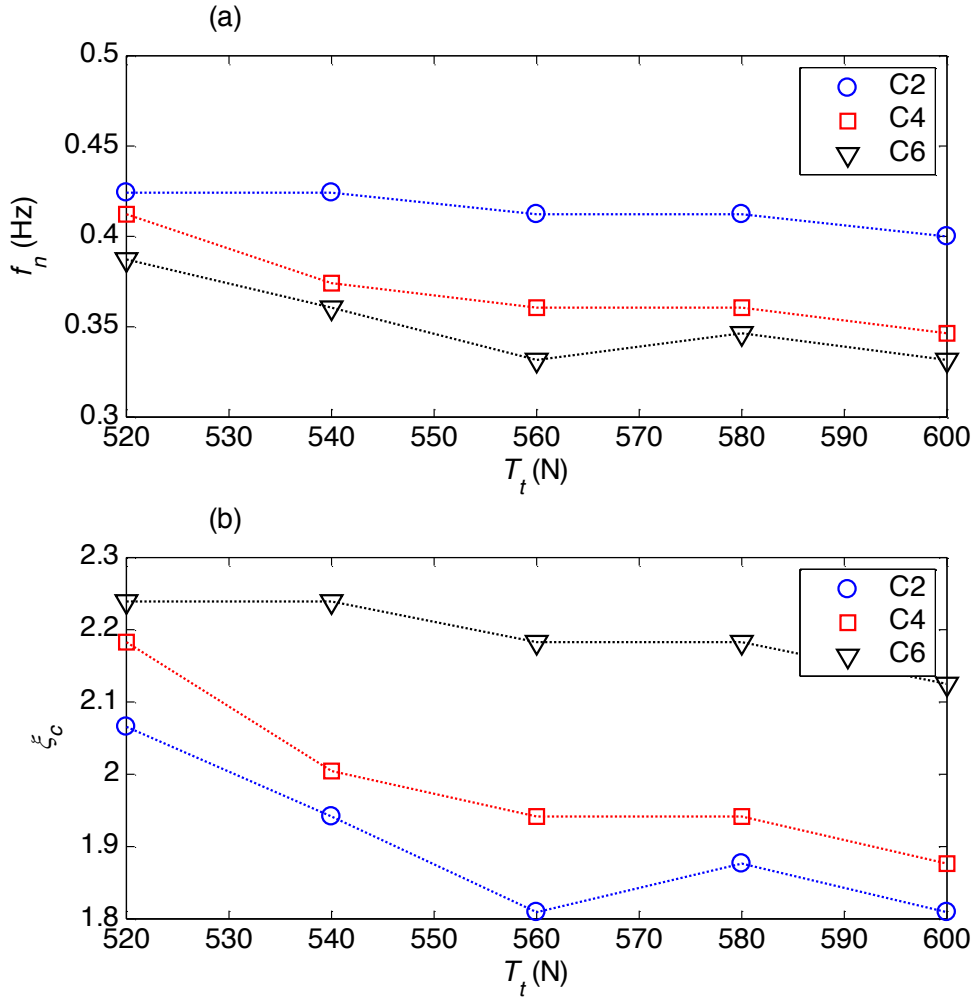
Figure 15. For all columns with EWM layers: (a) natural frequency, and (b) damping ratio.

5. Conclusions

In this study, the potential application of entangled wire materials in a novel composite bridge pier inspired by human spine was investigated. To achieve this goal, a number of displacement control tests and free-decay vibration tests were conducted on a small-scale column made from wooden blocks as vertebrae and entangled wire material layers as intervertebral discs, tied together by a stainless tendon. The in-plane rocking acceleration at the top of the column and tension force of the tendon were then collected for different arrangements of entangled wire material layers.

It is found that the column without any material between blocks is an oscillatory underdamped system while adding entangled wire material layers makes the column highly overdamped. Furthermore, it is found from the displacement control and free-decay vibration test results that the use of entangled wire materials significantly reduces the column's dynamic stiffness or frequency, and the column moves back to its initial state within a few cycles of vibration.

While the energy-dissipation capacity of entangled wire materials was found to be very promising for their potential use in future large-scale tests of the column, large shear deformations of the EWM layers were observed during testing which created significant drift ratios. Therefore, a material with optimal energy dissipation capacity and shear stiffness is fit for purpose as it dissipates rocking motion with causing less drift ratios.

Acknowledgement

REFERENCES

[1]   Guo A, Liu Z, Li S, Li H. Seismic performance assessment of highway bridge networks considering post-disaster traffic demand of a transportation system in emergency conditions. Structure and Infrastructure Engineering 2017;13:1523–37. doi:10.1080/15732479.2017.1299770.

[2]   Rokneddin K, Ghosh J. The Effects of Deteriorating Bridges on Bridges on the Bridge Network Connectivity. In 2011 Structures Congress., 2011. doi:10.1061/41171(401)260.

[3]   Liu M, Frangopol DM. Balancing connectivity of deteriorating bridge networks and long-term maintenance cost through optimization. Journal of Bridge Engineering 2005;10:468–81. doi:10.1061/(ASCE)1084-0702(2005)10:4(468).

[4]   ASCE. ASCE: Infrastructure Fact Sheet,. 2009.

[5]   Kashani MM, Lowes LN, Crewe AJ, Alexander NA. Computational modelling strategies for nonlinear response prediction of corroded circular RC bridge piers. Advances in Materials Science and Engineering 2016;2016. doi:10.1155/2016/2738265.

[6]   Kashani MM, Crewe AJ, Alexander NA. Structural capacity assessment of corroded RC bridge piers. Proceedings of the Institution of Civil Engineers - Bridge Engineering 2017;170:28–41. doi:10.1680/jbren.15.00023.

[7]   Ni Choine M, Kashani MM, Lowes LN, O'Connor A, Crewe AJ, Alexander NA. Nonlinear dynamic analysis and seismic fragility assessment of a corrosion damaged integral bridge. International Journal of Structural Integrity 2016;7:227–39. doi:10.1108/IJSI-09-2014-0045.

[8]   Dizaj EA, Madandoust R, Kashani MM. Probabilistic seismic vulnerability analysis of corroded reinforced concrete frames including spatial variability of pitting corrosion. *Soil Dynamics and Earthquake Engineering* 2018;114: 97-112.doi: 10.1016/j.soildyn.2018.07.013.

[9]   Kashani MM, Alagheband P, Khan R, Davis S. Impact of corrosion on low-cycle fatigue degradation of reinforcing bars with the effect of inelastic buckling. International Journal of Fatigue 2015;77:174–85. doi:10.1016/j.ijfatigue.2015.03.013.

[10]   Jara M, Jara JM, Olmos BA. Seismic energy dissipation and local concentration of damage in bridge bents. Structure and Infrastructure Engineering 2013;9:794–805. doi:10.1080/15732479.2011.615330.

[11]   Faecke A, Baur M, Schlueter FH, Thoma K. Assessment of Bridge Performance - Seismic Isolation versus Ductility. BAUINGENIEUR 2009;84:S7–12.

[12]   Dazio A. Residual Displacements in Capacity Designed Reinforced Concrete Structures. Proceedings of the 13th World Conference on Earthquake Engineering, 2004.

[13]   Qinghua AI, Dongsheng W, Hongnan LI, Zhiguo SUN. Evaluation of the Seismic Performance of Reinforced Concrete Bridge Columns Based on Plastic Hinge Model. 14th World Conference of Earthquake Engineering 2008:1–8.

[14]   Kim TH, Lee KM, Chung YS, Shin HM. Seismic damage assessment of reinforced concrete bridge columns. Engineering Structures 2005;27:576–92. doi:10.1016/j.engstruct.2004.11.016.

[15]   Khan MA. Accelerated Bridge Construction. Accelerated Bridge Construction 2015:257–308. doi:10.1016/B978-0-12-407224-4.00006-X.

[16]   Tazarv M, Saiid Saiidi M. Low-Damage Precast Columns for Accelerated Bridge Construction in High Seismic Zones. Journal of Bridge Engineering 2016;21:4015056. doi:10.1061/(ASCE)BE.1943-5592.0000806.

[17]   Khaleghi B. Highways for Life Projects and Accelerated Bridge Construction in Washington State. Trb 2011;7181:1–12.

[18]   Haber ZB. Precast Column-Footing Connections for Accelerated Bridge Construction in Seismic Zones. ProQuest Dissertations and Theses 2013:661.

[19]   Shim CS, Chung CH, Kim HH. Experimental evaluation of seismic performance of precast segmental bridge piers with a circular solid section. Engineering Structures 2008;30:3782–92. doi:10.1016/j.engstruct.2008.07.005.

[20]   Roh H, Reinhorn AM. Hysteretic behavior of precast segmental bridge piers with superelastic shape memory alloy bars. Engineering Structures 2010;32:3394–403. doi:10.1016/j.engstruct.2010.07.013.

[21]   Dawood H, ElGawady M, Hewes J. Behavior of Segmental Precast Posttensioned Bridge Piers under Lateral Loads. Journal of Bridge Engineering 2012;17:735–46. doi:10.1061/(ASCE)BE.1943-5592.0000252.

[22] Jia J-F, Zhao J-Y, Zhang Q, Han Q, Du X-L, Qi L-K. Cyclic Testing on Seismic Behavior of Precast Segmental CFST Bridge Piers with Bolted Connections. Zhongguo Gonglu Xuebao/China Journal of Highway and Transport 2017;30.

[23] Billington SL, Barnes RW, Breen JE. Alternate Substructure Systems for Standard Highway Bridges. Journal of Bridge Engineering 2001;6:87–94. doi:doi:10.1061/(ASCE)1084-0702(2001)6:2(87).

[24] Cheng C. Energy dissipation in rocking bridge piers under free vibration tests. Earthquake Engineering & Structural Dynamics 2007;36:503–18. doi:10.1002/eqe.640.

[25] Motaref S, Saiidi MS, Sanders D. Shake Table Studies of Energy-Dissipating Segmental Bridge Columns. Journal of Bridge Engineering 2014;19:186–99. doi:10.1061/(ASCE)BE.1943-5592.0000518.

[26] Nikbakht E, Rashid K, Hejazi F, Osman SA. Application of shape memory alloy bars in self-centring precast segmental columns as seismic resistance. Structure and Infrastructure Engineering 2015;11:297–309. doi:10.1080/15732479.2013.876056.

[27] Sideris P. Nonlinear quasi-static analysis of hybrid sliding-rocking bridge columns subjected to lateral loading. Engineering Structures 2015;101:125–37. doi:10.1016/j.engstruct.2015.06.053.

[28] Sideris P, Aref AJ, Filiatrault A. Quasi-Static Cyclic Testing of a Large-Scale Hybrid Sliding-Rocking Segmental Column with Slip-Dominant Joints. Journal of Bridge Engineering 2014;19:4014036. doi:10.1061/(ASCE)BE.1943-5592.0000605.

[29] Sideris P, Aref AJ, Filiatrault A. Experimental seismic performance of a hybrid sliding – rocking bridge for various specimen configurations and seismic loading conditions. Journal of Bridge Engineering 2015;20:1–15. doi:10.1061/(ASCE)BE.1943-5592.0000742.

[30] Sideris P, Aref AJ, Filiatrault A. Large-Scale Seismic Testing of a Hybrid Sliding-Rocking Posttensioned Segmental Bridge System. Journal of Structural Engineering 2014;140:4014025. doi:10.1061/(ASCE)ST.1943-541X.0000961.

[31] Salehi M, Sideris P, Liel AB. Numerical Simulation of Hybrid Sliding-Rocking (HSR) Columns subjected to Earthquake Excitation. Journal of Structural Engineering 2017;143:1–14. doi:10.1061/(ASCE)ST.1943-541X.0001878.

[32] Nikoukalam MT, Sideris P. Resilient Bridge Rocking Columns with Polyurethane Damage-Resistant End Segments and Replaceable Energy-Dissipating Links. Journal of Bridge Engineering 2017;22:4017064. doi:10.1061/(ASCE)BE.1943-5592.0001069.

[33] Kashani MM, Gonzalez-Buelga A. Nonlinear dynamics of self-centring segmental composite rocking column. Procedia Engineering 2017;199:441–6. doi:10.1016/j.proeng.2017.09.176.

[34] Zhang D, Scarpa F, Ma Y, Boba K, Hong J, Lu H. Compression mechanics of nickel-based superalloy metal rubber. Materials Science and Engineering A 2013;580:305–12. doi:10.1016/j.msea.2013.05.064.

[35] Hong J, Chen LL, Ma Y, Tomlinson GR, Rongong JA. Hysteretic properties of metal rubber particles. Proceedings of the Institution of Mechanical Engineers, Part C: Journal of Mechanical Engineering Science 2013;227:693–702. doi:10.1177/0954406212452380.

[36] Zhang D, Scarpa F, Ma Y, Hong J, Mahadik Y. Dynamic mechanical behavior of nickel-based superalloy metal rubber. Materials and Design 2014;56:69–77. doi:10.1016/j.matdes.2013.10.088.

[37] Chung T, Scarpa F. Shear dynamic behaviour of metal rubber as the core of artificial intervebral disc, AENGM0032 Research Project, Bristol University, Department of Aerospace Engineering. 2015.

[38] Carfagni M, Lenzi E, Pierini M. The loss factor as a measure of mechanical damping. SPIE Proceedings Series 1998:580–4.

[39] Zhang Q, Zhang D, Dobah Y, Scarpa F, Fraternali F, Skelton RE. Tensegrity cell mechanical metamaterial with metal rubber. Applied Physics Letter 2018;31906. doi:https://doi.org/10.1063/1.5040850.

[40] Ma Y, Zhang Q, Dobah Y, Scarpa F, Fraternali F, Skelton RE, et al. Meta-tensegrity: Design of a tensegrity prism with metal rubber. Composite Structures 2018;206. doi:https://doi.org/10.1016/j.compstruct.2018.08.067.

[41] Levin SM. The tensegrity-truss as a model for spine mechanics. Journal of Mechanics in Medicine and Biology 2002;2:375–88. doi:10.1142/S0219519402000472.

[42] Fabbrocino F, Carpentieri G. Three-dimensional modeling of the wave dynamics of tensegrity lattices. Composite Structures 2017;173:9–16. doi:10.1016/j.compstruct.2017.03.102.

[43] Amendola A, Carpentieri G, de Oliveira M, Skelton RE, Fraternali F. Experimental investigation of the softening-stiffening response of tensegrity prisms under compressive loading. Composite Structures 2014;117:234–43. doi:10.1016/j.compstruct.2014.06.022.

[44] Fraternali F, Carpentieri G, Modano M, Fabbrocino F, Skelton RE. A tensegrity approach to the optimal reinforcement of masonry domes and vaults through fiber-reinforced composite materials. Composite Structures 2015;134:247–54. doi:10.1016/j.compstruct.2015.08.087.

[45] Londoño JM, Neild SA, Cooper JE. Identification of backbone curves of nonlinear systems from resonance decay responses. Journal of Sound and Vibration 2015;348:224–38. doi:10.1016/j.jsv.2015.03.015.

[46] Renson L, Gonzalez-Buelga A, Barton DAW, Neild SA. Robust identification of backbone curves using control-based continuation. Journal of Sound and Vibration 2016;367:145–58. doi:10.1016/j.jsv.2015.12.035.

[47] Wagg D, Neild S, To CWS, Lau SK. Nonlinear Vibration with Control: For Flexible and Adaptive Structures. Springer Cham Heidelberg New York Dordrecht London; 2010. doi:10.3397/1.3455047.

[48] Worden K, Tomlinson G. Nonlinearity in Structural Dynamics: Detection , Identification and Modelling. Institute of Physics Publishing Bristol and Philadelphia; 2001.

[49] RDP group, http://www.rdpe.com n.d.

[50] PCB Piezotronics, http://www.pcb.com n.d.

[51] Simulink, MATLAB, Design, Simulation and Model-Based, Https://au.mathworks.com/products/simulink.html 2014.

[52] Touzé C, Thomas O, Chaigne A. Hardening/softening behaviour in non-linear oscillations of structural systems using non-linear normal modes. Journal of Sound and Vibration 2004;273:77–101. doi:10.1016/j.jsv.2003.04.005.

[53] Alexander NA, Oddbjornsson O, Taylor CA, Osinga HM, Kelly DE. Exploring the dynamics of a class of post-tensioned, moment resisting frames. Journal of Sound and

Vibration 2011;330:3710–28. doi:10.1016/j.jsv.2011.02.016.

[54]   Yu B, Gabriel D, Noble L, An KN. Estimate of the optimum cutoff frequency for the Butterworth low-pass digital filter. Journal of Applied Biomechanics 1999;15:318–29. doi:10.1123/jab.15.3.318.

[55]   Inman DJ. Vibration with control. John Wiley & Sons; 2017. doi:10.1037/023990.

[56]   Ahmadi E, Živanović S, Caprani C, Evans N, Heirdapour A. A framework for quantification of human-structure interaction in vertical direction. Journal of Sound and Vibration 2018;432. doi:10.1016/j.jsv.2018.06.054.